PROCEEDINGS OF SPIE

LED-based hyperspectral endoscopic imaging

Modir, Naeeme, Shahedi, Maysam, Dormer, James, Ma, Ling, Ghaderi, Mohammadaref, et al.

SPIE.

LED-based Hyperspectral Endoscopic Imaging

Naeeme Modir [a], Maysam Shahedi [a], James Dormer [a], Ling Ma [a],
Mohammadaref Ghaderi [a], Shashank Sirsi [a], Yi-Shing Lisa Cheng [b], Baowei Fei [a,c,*]

[a] Center for Imaging and Surgical Innovation
Department of Bioengineering, University of Texas at Dallas, Richardson, TX
[b] Department of Diagnostic Sciences, College of Dentistry, Texas A&M University, Dallas, TX
[c] Department of Radiology, University of Texas Southwestern Medical Center, Dallas, TX

* Email: bfei@utdallas.edu, Website: https://fei-lab.org

ABSTRACT

Hyperspectral endoscopy can offer multiple advantages as compared to conventional endoscopy. Our goal is to design and develop a real-time hyperspectral endoscopic imaging system for the diagnosis of gastrointestinal (GI) tract cancers using a micro-LED array as an in-situ illumination source. The wavelengths of the system range from ultraviolet to visible and near infrared. To evaluate the use of the LED array for hyperspectral imaging, we designed a prototype system and conducted *ex vivo* experiments using normal and cancerous tissues of mice, chicken, and sheep. We compared the results of our LED-based approach with our reference hyperspectral camera system. The results confirm the similarity between the LED-based hyperspectral imaging system and the reference HSI camera. Our LED-based hyperspectral imaging system can be used not only as an endoscope but also as a laparoscopic or handheld devices for cancer detection and surgery.

Keywords: Hyperspectral imaging, endoscopy, laparoscope, handheld device, micro-LED, cancer, surgery, FPGA

1. INTRODUCTION

In 2021, digestive system cancers were the most common cancers in the United States with 338,090 and 169,280 estimated incidences and mortalities, respectively[1]. The current gold standard for the diagnosis of gastrointestinal (GI) cancers is endoscopy. However, conventional endoscopy uses RGB (red-green-blue) light for imaging and therefore suffers from low sensitivity and low spectral resolution. Up to about 10% of the cancers are missed during conventional upper GI endoscopic examination due to the lack of visibility[2, 3].

Hyperspectral imaging (HSI) has shown to improve the diagnosis of cancerous tissue by improving the spectral resolution using different discrete wavelengths of light to capture the images[4-6]. Previous studies showed that GI cancer could be differentiated from normal tissues using HSI[7-10]. For a GI endoscopy application, a tiny high-resolution camera with a real-time imaging rate is required. However, commercial HSI systems have not been designed for GI endoscopy applications. For example, a majority of the commercially available hyperspectral (HS) cameras are either bulky or slow. Therefore, usually, a bundle of fiber optics is used to transfer light from an external light source into the imaging site inside the body and transfer the captured images to an external HS camera.

There are some previously proposed multi- and hyper-spectral endoscopes presented in the literature using fiber optics[11-13]. Lim *et al.*[12] used 100 optical fiberlets for a high-spectral (756 wavelengths) and low-spatial resolution (10 pixels × 10 pixels) snap-shot HSI. The field of view of their HSE is 1.1 mm × 1.3 mm and the HS imaging rate is 6 fps. Kester *et al.*[13] presented a snapshot HSE with a high spatial resolution (350 pixels × 350 pixels) and 48 spectral bands from 450 nm to 650 nm. The imaging rate of their system is about 5 fps. Han *et al.*[11] used a mechanical wheel to provide different wavelengths in a multispectral colonoscope. Their system is limited in the number of spectral bands (five bands). There are other HS endoscope designs presented in the literature that are limited by either the number of spectral bands[14] and/or the imaging rate[14, 15].

Some studies have characterized LED-based illumination sources for imaging systems. Shrestha *et al.*[16] used a simulation to investigate the performance of a multi-wavelength, LED-based, light source in multispectral imaging. They compared the quality of the images captured with a multiwavelength LED source and a monochrome camera to an RGB camera.

They showed that multispectral imaging with an LED light source results in a higher imaging quality but lower imaging rate.

Our objective is to develop an HSI endoscope (HSE) system using micro-LEDs with different wavelengths as the illumination source, a high-speed monochrome camera for image capturing, and an application-specific integrated circuit (ASIC) for controlling and data processing. Figure 1 shows a block diagram of the proposed system. In this paper, we have conducted a feasibility study to assess the imaging quality of the proposed HSE for potential medical adaptation. We implemented a prototype system using hole-through LEDs with different wavelengths and an FPGA for controlling the LEDs. Our feasibility study includes a set of experiments that evaluate the performance of the HSI system we developed based on in-situ LED illumination. We have studied the performance of the prototyped system on several normal and cancerous *ex vivo* tissues obtained from animal models.
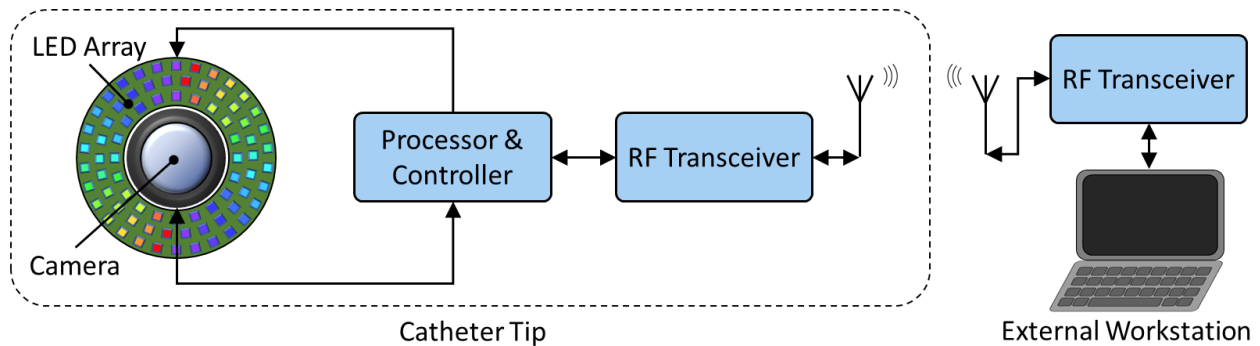

Figure 1. Block diagram of the micro-LED-based hyperspectral endoscopic imaging system.

2. MATERIALS AND METHODS

2.1 Hyperspectral imaging designs

Proposed hyperspectral endoscope system: Our proposed HSE uses a set of micro-LEDs with different wavelengths from ultra-violet (UV) to visible, near-infrared (NIR), and infrared (IR) as the light source. The system consists of two parts: (1) a catheter that goes inside the body to capture images from the GI tract, and (2) the external workstation for further processing of the captured images. The catheter consists of an LED array, a high-speed monochrome micro-camera, and all the electronic circuitries needed for controlling and processing. The LED array consists of up to 30 micro-LEDs with different wavelengths from 355 nm to 1200 nm with a spectral resolution of about 30 nm. The high-speed monochrome camera must have an imaging rate of up to 600 fps for a close to real-time HS image capturing rate (*i.e.,* 16 hypercube per second). An ASIC is used for controlling the micro-LEDs and the camera. A wireless transceiver communicates with the external workstation to receive the controlling comments and send the captured data. In this study, we investigated the feasibility of taking HS images using LEDs and a monochrome camera in a large-scale prototype system. We used the implemented prototype to conduct a series of experiments to characterize the LED-based HSI system.

Customized Prototype System: Our LED-based HSI prototype captures spectral images in 18 different wavelengths: 405, 420, 450, 470, 505, 525, 555, 590, 610, 630, 660, 700, 770, 800, 830, 850, 890, and 910 nm. To block environment lights, we implemented the LED array, the monochrome camera, and the imaging target inside a dark box. Figure 2 shows the setup of the system. A moving stage was used in the box to adjust the distance between the imaging sensor and the target. The LED array was mounted inside the dark box around the camera lens and in front of the moving stage to illuminate the target with the specific wavelength. For adjusting the forward voltages of the LEDs, we used one potentiometer in series with each LED in our setup. An FPGA was used to control the LEDs. The FPGA general-purpose I/Os were connected to the LEDs driving board to provide a controlling signal for turning on and off the LEDs. We used a diffuser film in front of the LED array to have a better distribution of the illumination.

2.2 System calibration

The LEDs' light intensity and distribution and the sensitivity of the camera sensor elements can be variable. Therefore, an image intensity calibration is required before each experiment to adjust the intensity of the spectral images. The calibration

compensates for the spatial and spectral inhomogeneity of the LEDs' illuminations and the spatial inhomogeneity in camera sensors. For calibration, we use (1) the image when there is no light (dark current) and (2) the reflected intensity from a white reference when only one of the LEDs is on. For L spectral bands (here $L = 18$), the calibrated image, $\hat{I}(x, y, \lambda)$, after canceling out the intra-wavelength inhomogeneous illumination distribution as well as inter-wavelength illumination inconsistency is given as:

$$\hat{I}(x, y, \lambda) = \frac{I(x, y, \lambda) - I_D(x, y)}{I_W(x, y, \lambda) - I_D(x, y)}, \quad \lambda \in \{1,2,3, \dots, L\}$$

where for each pixel (x, y), $I(x, y, \lambda)$ is the reflection intensity of the λth band of the hypercube before calibration, $I_D(x, y)$ is the reflection intensity of the dark image captured when all the LEDs are off, and $I_W(x, y, \lambda)$ is the reflection intensity of the λth band when a white reference is used as the target.

2.3 Experiments

For evaluating the performance of hyperspectral imaging using LED-based illumination, we designed a set of experiments on *ex vivo* tissues. We captured images of the tissues using our customized HSI camera system as the reference. The reference camera covered 150 wavelengths from 470 nm to 900 nm with a spectral resolution of about 3 nm. We compared the acquired spectral images to the reference HS image. For the *ex vivo* imaging, we used normal tissues taken from different animal models, including chicken (drumstick), lamb (brain, heart, liver, and kidney), and mice (heart, liver, left and right kidneys). We also used four neuroblastoma cancerous tissues from two mice for the *ex vivo* imaging. Before starting the experiments, we first captured an image with all the LEDs off and then captured images from a white reference for calibration purposes. For capturing images from each *ex vivo* tissue, we put the tissue on the stage inside the dark box and sealed the box to block the environmental light. Then we turned the first LED on for 2 seconds, captured the images, and then turned off the LED. With a delay of 2 seconds, the next LED was turned on. We continued to turn on and off the LEDs one by one and capture the images. Figure 2 shows the waveforms of the LEDs' driving signals provided by the FPGA evaluation board. The pulse width (PW) of the signals and the delay between every two sequential signals (DT) were 2 seconds. Figure 3 shows the setup of our HSI prototype and Figure 4 shows the imaging setup for the reference HSI camera.
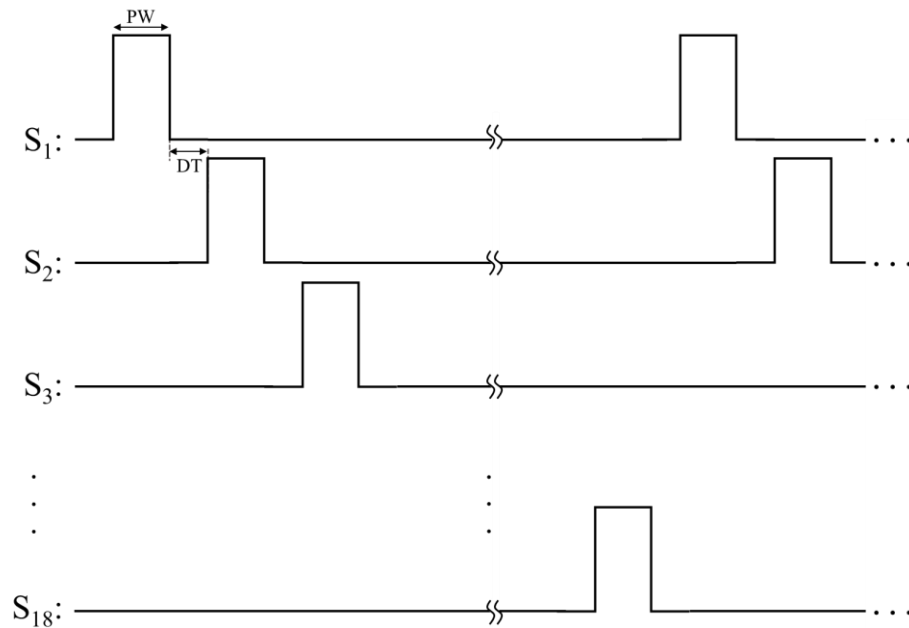

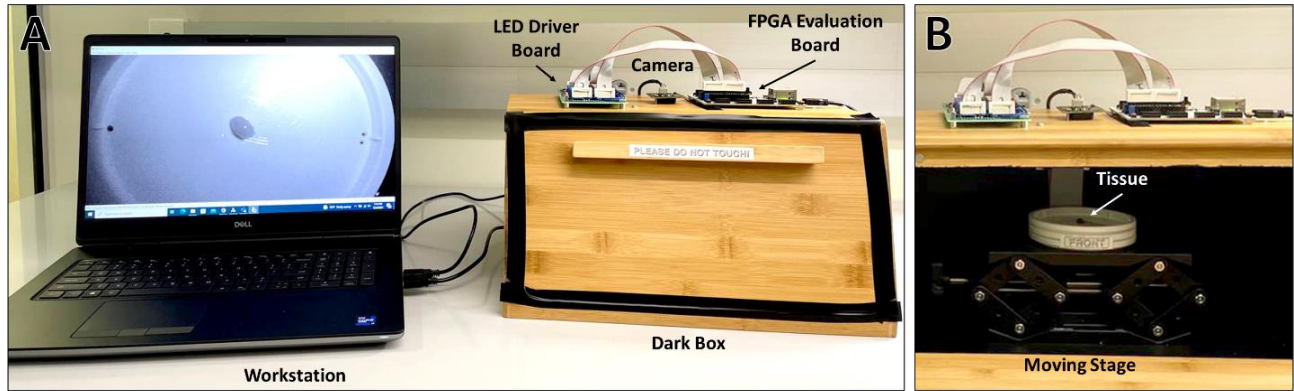**Figure 2.** Signals for the LED array driver and control of the system.

Figure 3. Experiment setup (A) and the dark box (B) for the *ex vivo* tissue imaging experiments.
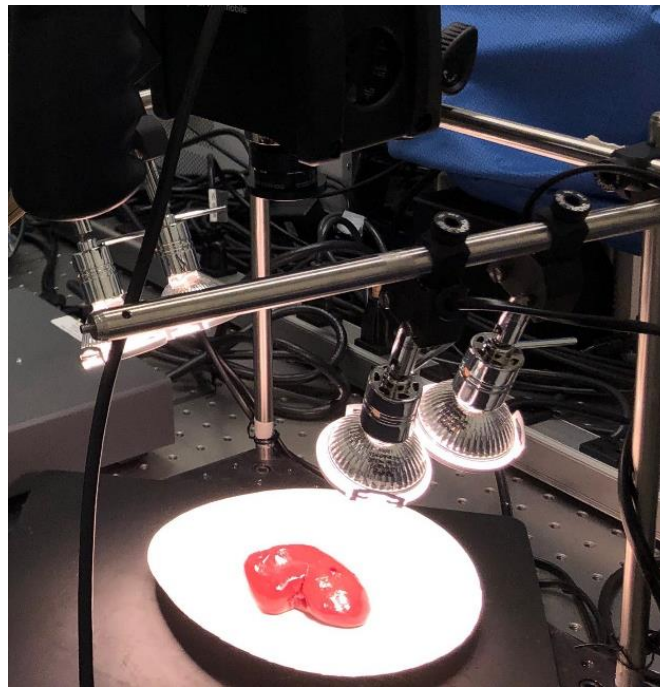

Figure 4. Imaging setup using our customized HSI camera system.

For each tissue, we calibrated the images captured by our LED-based HSI system and the reference HSI camera and then register the images from the reference camera to the images captured by our LED-based system. Then, we segmented the images automatically to remove the background and the glares of the images on each pair of hypercubes using a histogram analysis method. To combine the two segmented tissue masks, we used the overlap region between them. It resulted in a single segmentation mask showing the common region of interest (ROI) in both hypercubes. We applied our further processing within this ROI. We also extracted the spectral signatures of the tissues from the ROIs. To have a better comparison between the two systems we normalized the spectral signatures using the following equation:

$$\hat{S}(\lambda) = \frac{S(\lambda) - S_{min}}{S_{max} - S_{min}},$$

where $S(\lambda)$ is the original spectral signature at wavelength λ, S_{min} and S_{max} are the minimum and maximum values of $S(\lambda)$, respectively, and $\hat{S}(\lambda)$ is the normalized spectral signature.

3. RESULTS

Figure 5 shows the images of all the 18 spectral channels from the white template before and after the calibration. Before calibration, for each spectral band, the illumination level and distribution were different from the other bands. After, calibration, the corrected reflectance rates of all the pixels at all the spectral bands except one (610 nm) are the same and at the highest intensity level as expected for white reference images. For the 610 nm band, the angle of illumination of the LED was small and the LED light could not cover the whole field of view. Therefore, the right top corner of the band has been affected by an illumination artifact that could not be corrected during the calibration process. For those tissues that ROI was not within the affected region, the illumination artifact has no impact on the hyperspectral signatures. However, the hyperspectral signatures of tissues within the illumination artifact region could be affected at 610 nm. Figures 6 to 9 show the captured images from four selected *ex vivo* tissues including a normal mouse kidney, a normal mouse liver, a normal lamb brain, and an orthotopically implanted human neuroblastoma resected from a mouse model. The figures show eight sample spectral bands captured by the prototype system and the corresponding bands from the reference hypercube. For a better comparison between the two imaging systems, the intensities of each hypercube were normalized based on the corresponding HS signature of the tissue. These figures show that our system could capture images with comparable quality when compared to our customized HSI camera system. At lower wavelengths like 470 nm, the quality of the images of our system is even higher than the reference camera. Figures 10 and 11 show the spectral signatures of the normal tissues for both HSI systems. They show the capability of our system in differentiating between different tissues similar to the reference camera. Figure 12 compares the hyperspectral images of the two HSI systems for the four sample tissues shown in Figures 6 to 9. The spectral signatures were plotted at the overlap spectral range of the two systems and based on the corresponding wavelengths in that range. Figure 13 compares the spectral signatures of normal mouse tissues to neuroblastoma tumor signature using our HSI system. For each spectral band, we compared the reflection of the normal tissues to the cancerous ones using one-tailed student t-tests with a significance threshold level of 0.05. This figure shows that our system could differentiate between normal and cancerous tissues with statistically meaningful differences at five to six bands. We observed statistically significant differences between cancer and all the normal tissues at 505 nm and 660 nm.
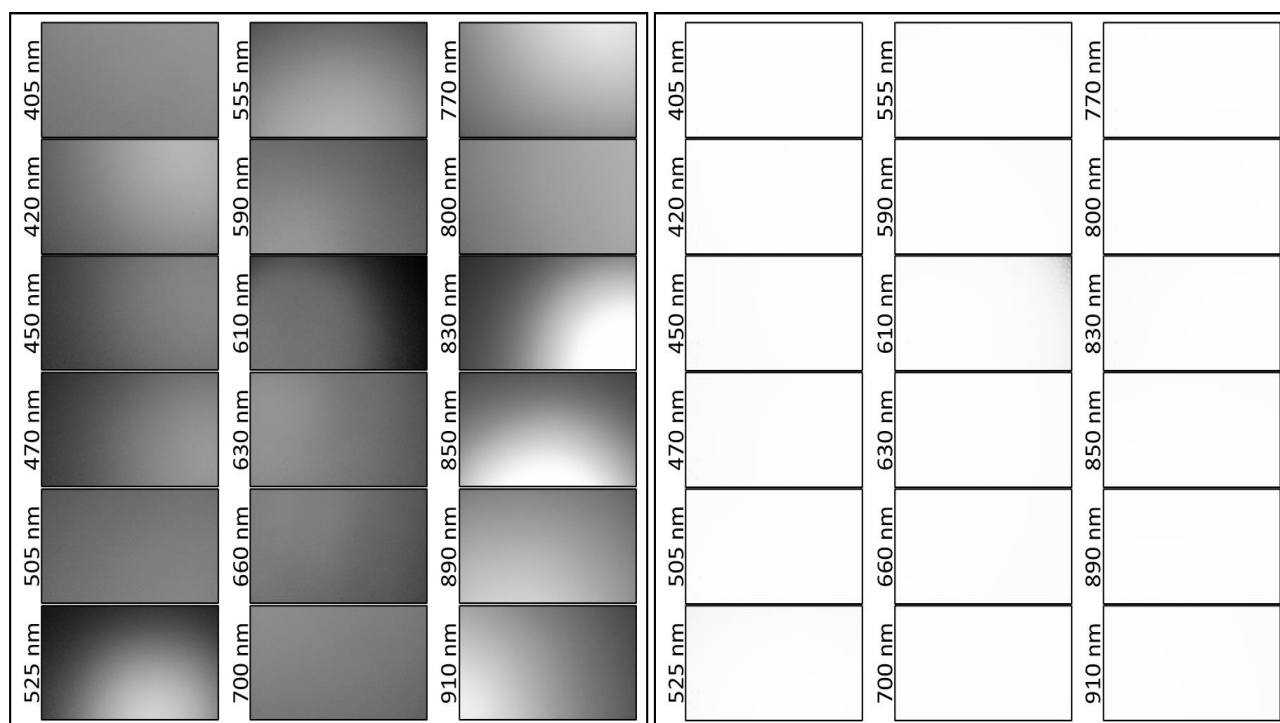

Figure 5. Spectral images of the white reference before calibration (left) and after calibration (right).
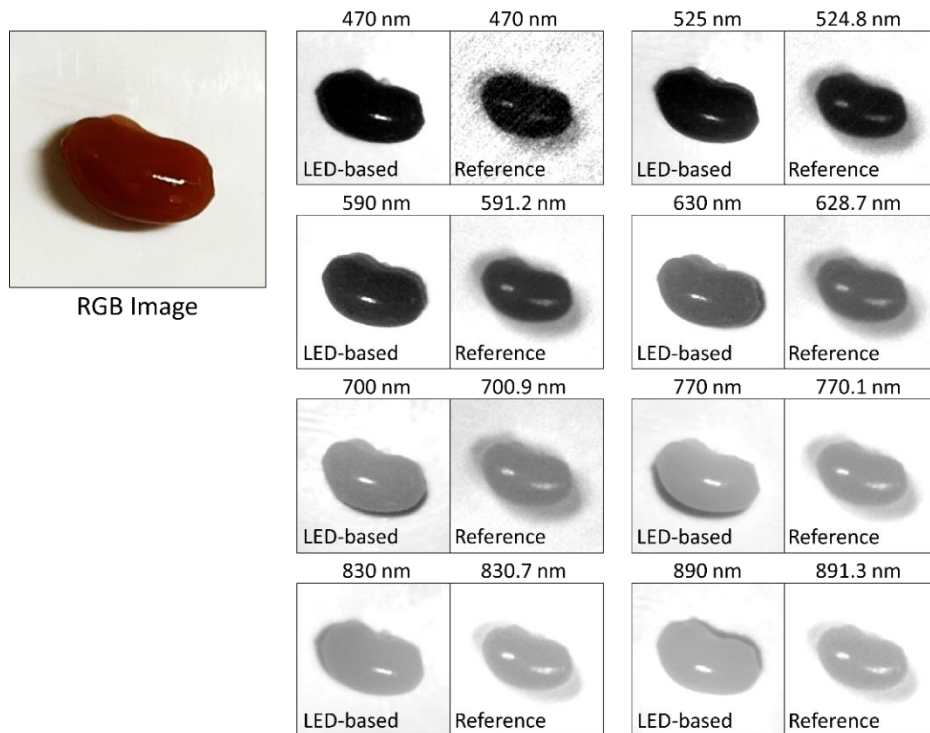
Figure 6. Spectral channels of our LED-based HSI prototype system (left images)
and the reference HSI camera (right images) from a normal mouse kidney at eight sample bands.
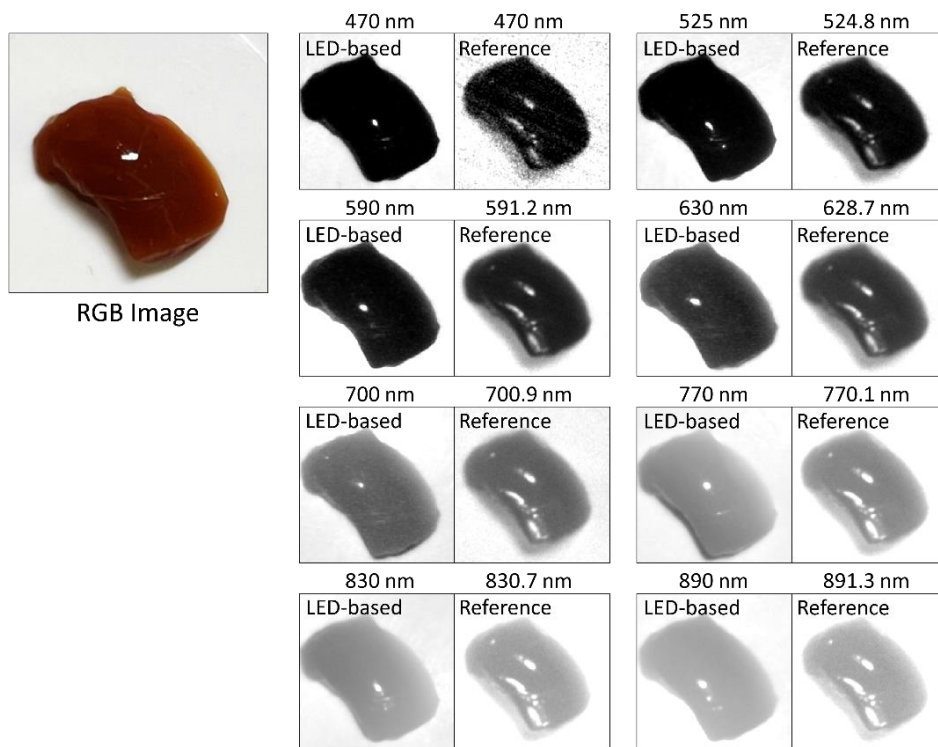

Figure 7. Spectral channels of our LED-based HSI prototype system (left images)
and the reference HSI camera (right images) from a normal mouse liver at eight sample bands.
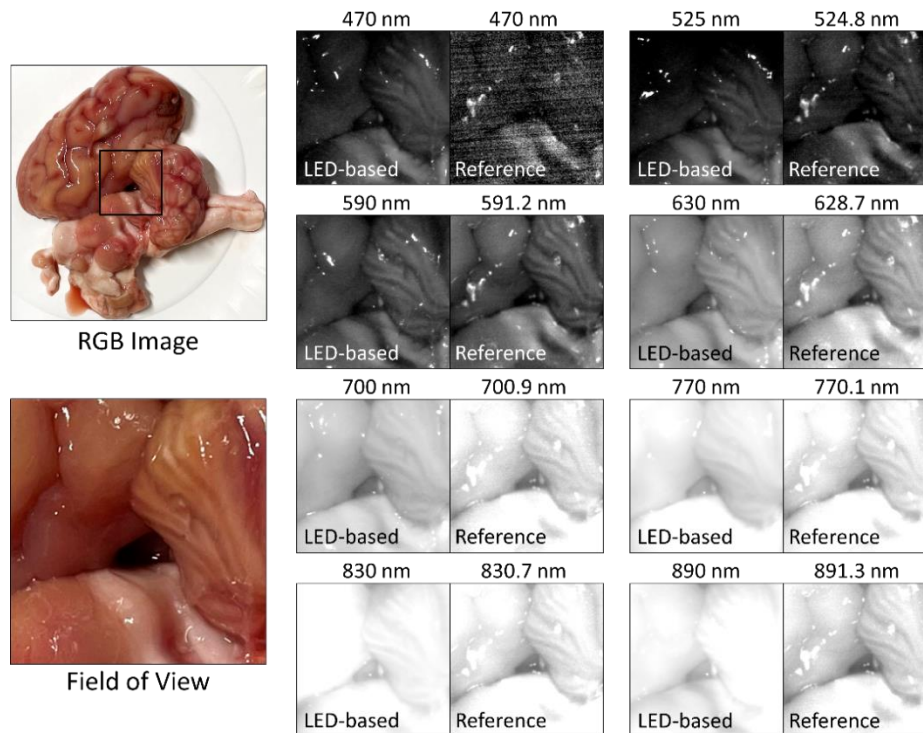
Figure 8. Spectral channels of our LED-based HSI prototype system (left images) and the reference HSI camera (right images) from a normal lamb brain at eight sample bands.
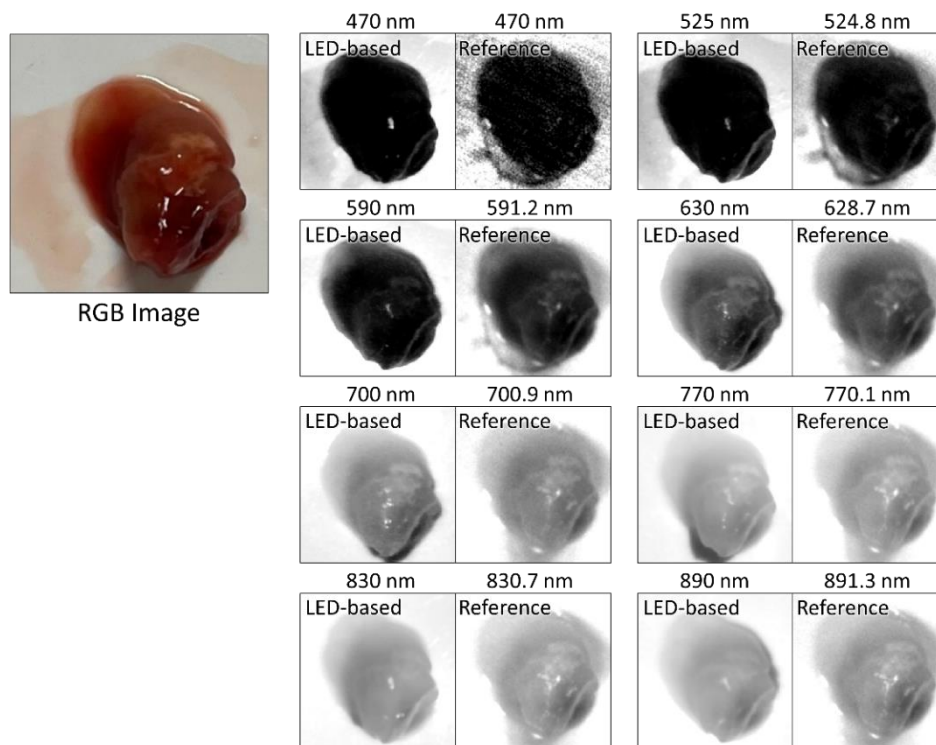

Figure 9. Spectral channels of our LED-based HSI prototype system (left images) and the reference HSI camera (right images) from a neuroblastoma tumor resected from a mouse model at eight sample bands.
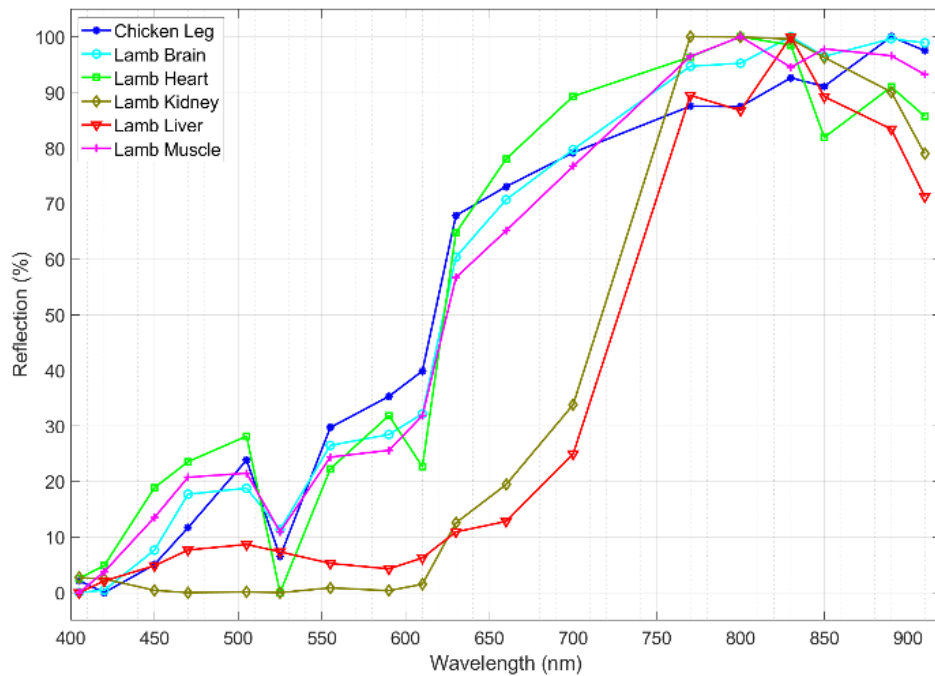
Figure 10. Spectral signatures of normal lamb and chicken tissues from our LED-based HSI system.
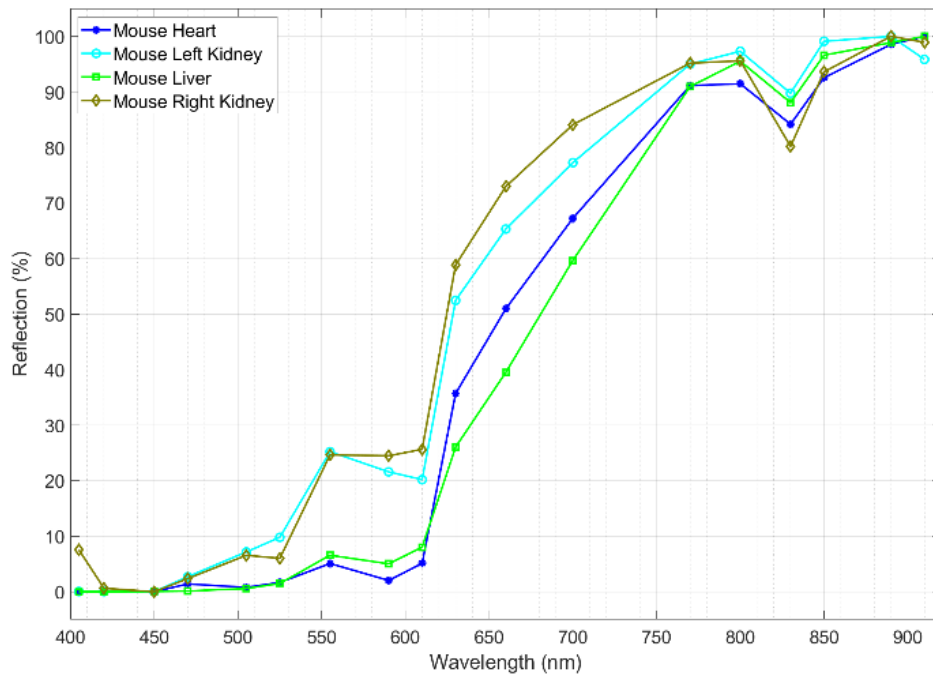

Figure 11. Spectral signatures of normal mouse tissues from our LED-based system.
The corresponding bands are shown with markers on the graphs.

4. DISCUSSION AND CONCLUSIONS

We have designed and developed a prototype of a wavelength scanning HSI system based on multi-wavelength LED illumination. We tested our HSI system on *ex vivo* tissues and compared the results of our LED-based HSI system to a reference HSI camera. Results show that the performance of our LED-based system is comparable to the reference HSI camera system. Based on our preliminary results, our LED-based hyperspectral imaging system detected statistically significant differences between normal and cancer at multiple spectral bands (see Figure 13). In some spectral bands, we observed a difference between the hyperspectral signatures of our system and that of the reference system (see Figure 12). This difference could be due to the imaging time delay between the two image acquisitions that resulted in different tissue conditions, such as tissue drying under the illumination of the reference camera system. Also, for those LEDs with low illumination powers or narrow viewing angle (*e.g.,* 525 nm, 610 nm, and 830 nm bands in Figure 5), the level of noise in the low-illumination region could be high, and the hyperspectral signature could be affected by noise at those bands. For example, in Figures 12A and 12B, the observed difference between the LED-based prototype and the reference camera at 830 nm could be justified by a high level of imaging noise. Although the calibration compensates for the low illumination, it cannot reduce the noise level at this band. A noise reduction process could be helpful to mitigate the noise effect on the hyperspectral signatures.
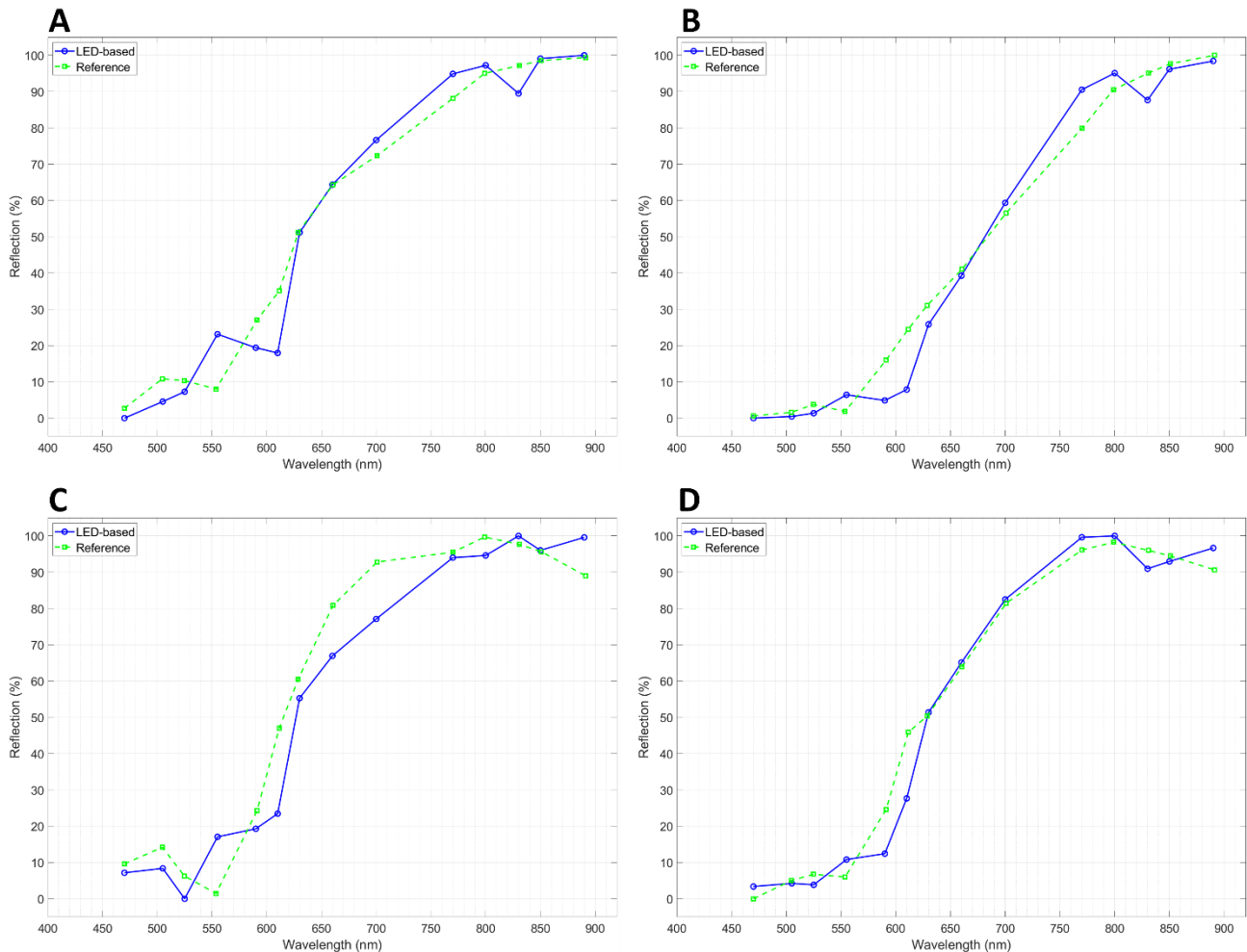

Figure 12. Spectral signature comparison between our LED-based HSI system and the reference system at corresponding wavelengths for the four sample tissues, which are shown in Figures 6 to 9. (A) Mouse kidney, (B) mouse liver, (C) lamb brain, and (D) neuroblastoma tumor.
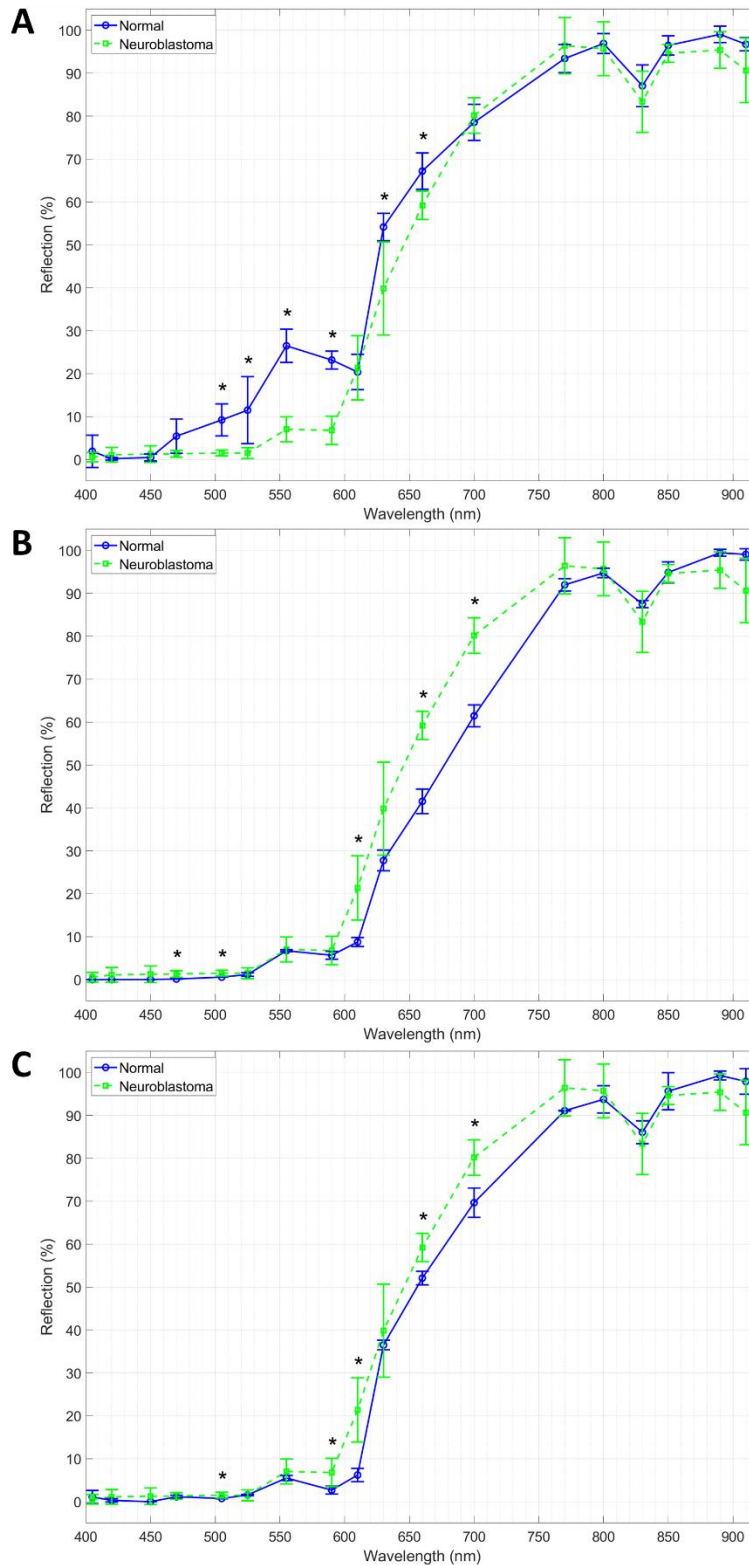
Figure 13. Comparison between spectral signatures of our LED-based HSI system for normal mouse tissues and neuroblastoma tumors. (A) Normal kidney, (B) normal liver, and (C) normal heart vs neuroblastoma tumor. The asterisk symbols show the spectral channels with statistically significant differences between the normal and cancerous tissues ($p < 0.05$).

In our prototype, a separate illumination source (LED) was used for each spectral band. Therefore, the illumination characteristics (*e.g.,* illumination power and distribution) of each band were different from the other bands. The calibration compensated for some of the inter-band inconsistency observed in this study. The glare pattern and location also changed from one channel to the other because of the different locations and angles of illumination of LEDs. In the real-size endoscope, we will use more than one LEDs per wavelength to address these issues. We will use optical simulation to optimize the location of each LED in the array to make the illumination uniform for each wavelength band.

In conclusion, we designed an LED-based hyperspectral imaging prototype system and studied the feasibility of using an LED-based illumination for fast and reliable hyperspectral imaging. The preliminary results show that the spectra of our hyperspectral imaging system are comparable to those of the reference hyperspectral camera. For future work, we will use micro-LEDs and a small high-speed monochrome camera to develop a miniature hyperspectral endoscope. We will design an ASIC for controlling the LEDs and camera to decrease the size, power consumption, and cost of the system. The LED-based hyperspectral imaging technique can be used not only for endoscopes but also for laparoscopes and handheld devices and can have wide applications in disease detection, diagnosis, and treatment.

ACKNOWLEDGMENT

REFERENCES

[1]   Siegel, R. L., Miller, K. D., Fuchs, H. E., and Jemal, A., "Cancer statistics, 2021," CA: a cancer journal for clinicians, 71(1), 7-33 (2021).

[2]   Menon, S., and Trudgill, N., "How commonly is upper gastrointestinal cancer missed at endoscopy? A meta-analysis," Endoscopy international open, 2(2), E46 (2014).

[3]   Chadwick, G., Groene, O., Riley, S., Hardwick, R., Crosby, T., Hoare, J., Hanna, G. B., Greenaway, K., and Cromwell, D. A., "Gastric cancers missed during endoscopy in England," Clinical gastroenterology and hepatology, 13(7), 1264-1270. e1 (2015).

[4]   Lu, G., and Fei, B., "Medical hyperspectral imaging: a review," Journal of biomedical optics, 19(1), 010901 (2014).

[5]   Halicek, M., Fabelo, H., Ortega, S., Callico, G. M., and Fei, B., "In-vivo and ex-vivo tissue analysis through hyperspectral imaging techniques: revealing the invisible features of cancer," Cancers, 11(6), 756 (2019).

[6]   Fei, B., Lu, G., Wang, X., Zhang, H., Little, J. V., Patel, M. R., Griffith, C. C., El-Diery, M. W., and Chen, A. Y., "Label-free reflectance hyperspectral imaging for tumor margin assessment: a pilot study on surgical specimens of cancer patients," Journal of biomedical optics, 22(8), 086009 (2017).

[7]   Liu, N., Guo, Y., Jiang, H., and Yi, W., "Gastric cancer diagnosis using hyperspectral imaging with principal component analysis and spectral angle mapper," Journal of Biomedical Optics, 25(6), 066005 (2020).

[8]   Akbari, H., Uto, K., Kosugi, Y., Kojima, K., and Tanaka, N., "Cancer detection using infrared hyperspectral imaging," Cancer science, 102(4), 852-857 (2011).

[9]   Akbari, H., Halig, L., Schuster, D. M., Fei, B., Osunkoya, A., Master, V., Nieh, P., and Chen, G., "Hyperspectral imaging and quantitative analysis for prostate cancer detection," Journal of biomedical optics, 17(7), 076005 (2012).

[10]   Halicek, M., Dormer, J. D., Little, J. V., Chen, A. Y., Myers, L., Sumer, B. D., and Fei, B., "Hyperspectral imaging of head and neck squamous cell carcinoma for cancer margin detection in surgical specimens from 102 patients using deep learning," Cancers, 11(9), 1367 (2019).

[11]   Han, Z., Zhang, A., Wang, X., Sun, Z., Wang, M. D., and Xie, T., "In vivo use of hyperspectral imaging to develop a noncontact endoscopic diagnosis support system for malignant colorectal tumors," Journal of biomedical optics, 21(1), 016001 (2016).

[12]   Lim, H.-T., and Murukeshan, V. M., "A four-dimensional snapshot hyperspectral video-endoscope for bio-imaging applications," Scientific reports, 6(1), 1-10 (2016).

[13] Kester, R. T., Bedard, N., Gao, L. S., and Tkaczyk, T. S., "Real-time snapshot hyperspectral imaging endoscope," Journal of biomedical optics, 16(5), 056005 (2011).

[14] Dung, L.-R., and Wu, Y.-Y., "A wireless narrowband imaging chip for capsule endoscope," IEEE Transactions on Biomedical Circuits and Systems, 4(6), 462-468 (2010).

[15] Shapey, J., Xie, Y., Nabavi, E., Bradford, R., Saeed, S. R., Ourselin, S., and Vercauteren, T., "Intraoperative multispectral and hyperspectral label-free imaging: A systematic review of in vivo clinical studies," Journal of biophotonics, 12(9), e201800455 (2019).

[16] Shrestha, R., and Hardeberg, J. Y., "How are LED illumination based multispectral imaging systems influenced by different factors?," International Conference on Image and Signal Processing. 61-71 (2014).